Dato: 2016-12-18

REPORT 20/2016
ISBN 978-82-7492-343-0
ISSN 1890-5226

S1+CS FEASIBILITY STUDY

Assessment of wind/wave/current retrieval methodology

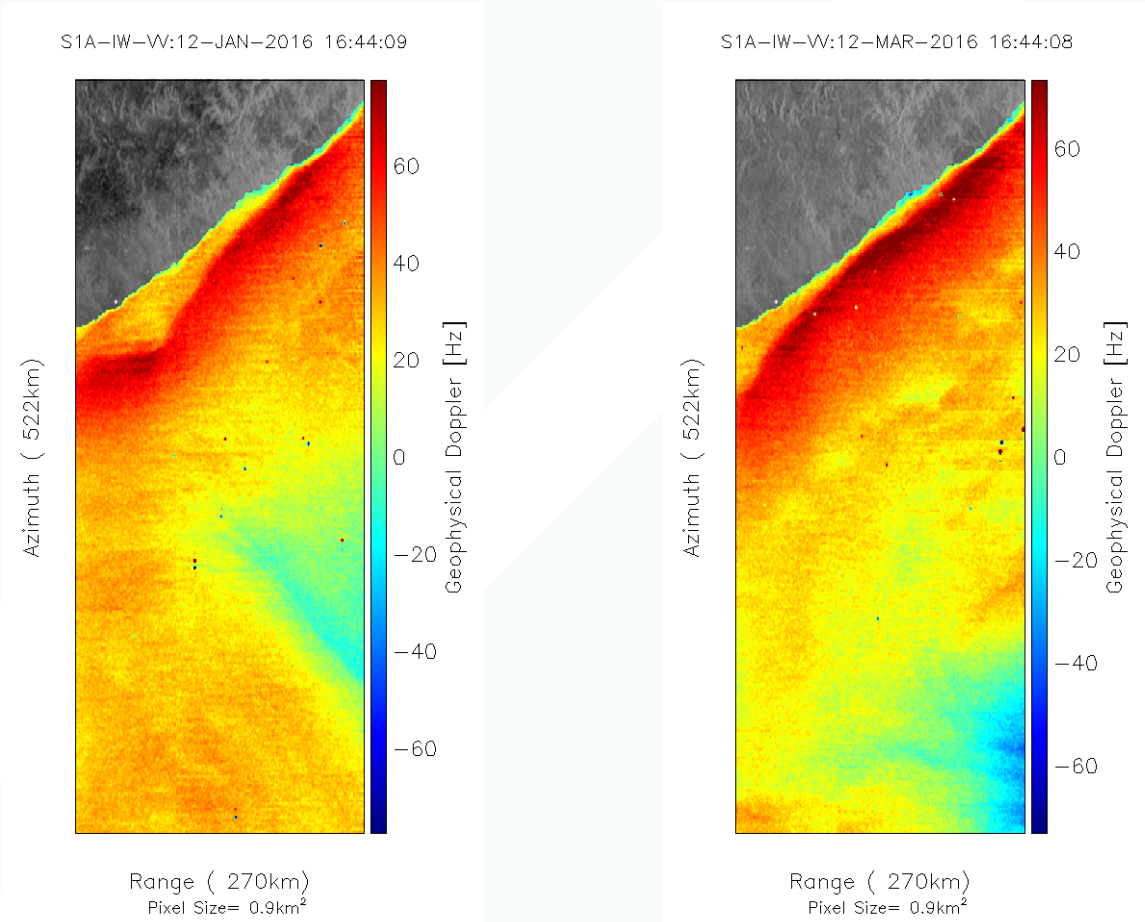

Author: Harald Johnsen

P.O. BOX 6434, TROMSØ SCIENCE PARK
N-9294 TROMSØ, NORWAY
TEL: +47 77 62 94 00, FAX: +47 77 62 94 01
post@norut.no
www.norut.no

norut
NORTHERN RESEARCH INSTITUTE

Project name: S1+CS **Project No.: 657**

Contractor (s): Contract ref.:

Document No.: 20/2016, v1.1 Document Type: Report Status: Open

ISBN: 978-82-7492-343-0 ISSN: 1890-5226 No. Pages: 28

Project manager: Harald Johnsen Dato: 2016-12-18

Author (s): Harald Johnsen

S1 + CS Feasibility Study - Assessment of wind/wave/current retrieval methodology

Resymé / Summary:

This work is done as part of a CCN related to the S1+CS study performed by Airbus Defence & Space for the European Space Agency.

The document gives a high-level description of possible wind/wave/current retrieval methodologies from S1+CS StereoSAR measurement, and recommendation for future detail study on the topic. Recent experience with and performance of the Sentinel 1 Doppler measurements are included in the document.

The version 1.0 of the document has an updated version of Section 2.1.1, including a new Figure 4 , Figure 5 and an updated Figure 6.

In the last version of the document (version 1.1) a new section (Section 2.1.2) is added describing the latest results of the Doppler analysis of Sentinel 1b data.

Keywords: SAR, Sentinel 1, bi-static, ocean surface current, ocean surface wind

Notes:

Publisher: Norut

Content:

Abbreviations:

- ATBD – Algorithm Theoretical Basis Document
- CDOP – C-band Doppler Model
- CMOD – C-band Geophysical Model Function
- C-SARMOD - C-band SAR Geophysical Model Function
- DC - Doppler Centroid
- DCA - Doppler Centroid Anomaly
- TOPS – Terrain Observation by Progressive Scan
- S1 – Sentinel 1A, Sentinel 1B
- SAR – Synthetic Aperture Radar
- SLC – Single-Look-Complex
- PRF – Pulse Repetion Frequency
- NRCS – Normalized Radar Cross Section
- OSC - Ocean Surface Current
- GCM - Generalized Curvature Ocean Surface Scattering Model

1. Background

Mapping of ocean surface wind, waves and current from space are important inputs to improve the characterization and parameterizations of oceanic dynamics as well as support to advances in ocean-atmosphere research and modeling activities. With the launch of the Sentinels, the capabilities of providing such high-resolution information from space is significantly improved due to dedicated processing algorithms, better time/space coverage and data quality. However, fundamental limitations with mono-static SAR observation geometry has led to the investigation of possible passive Sentinel follower in bi-static geometry for measuring ocean surface current [31].

1.1. Doppler Anomaly and Radial Velocity

The Doppler centroid anomaly (DCA) recorded over ocean with a Synthetic Aperture Radar (SAR) can be used to obtain range directed velocity which has been demonstrated to provide valuable estimates of the near surface wind speed, ocean surface current [1],[2],[2] and sea ice sea drift [4]. The Doppler centroid (DC) frequency recorded over ocean differs from the geometric and instrument Doppler centroids arising from satellite orbit/attitude and antenna miss pointing, respectively. This difference, called the Doppler centroid anomaly (or geophysical Doppler), is a direct measure of the line-of-sight (radial) velocity of the moving ocean surface. The DCA is thus highly sensitive to the motion of the scatterers induced by the surface currents (Ekman, tidal, geostrophic), and winds in combination with the orbital motion of the ocean waves (wind drift, Stokes drift). Despite the potential of Sentinels to measure ocean surface currents, there are limitations and several challenges related to the utilization of these measurements such as:

- The range of DCA is relatively small, only between –60 and +60Hz
- The contribution to the Doppler centroid from antenna and satellite attitude/orbit can be more than the geophysical signal, and difficult to predict to the required accuracy
- Means of accurate calibration of the Doppler signal

- A geophysical model function (GMF) capable of describing and separating the geophysical processes that contributes to the DCA
- The DCA from a mono-static SAR provides only line-of-sight component of the surface velocity field

Any retrieval of the underlying ocean surface current from DCA measurements requires the prediction and removal of all contributions arising from wind and waves. The net velocity induced by the near surface wind is interpreted as the mean line-of-sight velocity that the radar detected scatter elements feel when riding on the longer waves. As the scatter elements are tilted by longer waves, the NRCS varies along the wave profiles due to modulation effects (tilt- and hydrodynamic), leading to correlation with horizontal and vertical orbital velocities. It is basically through the modulation that the polarization and incidence angle dependencies enter into the expression for the Doppler anomaly. A clear physical interpretation and explanation of this can be found in [1]. A further theoretical derivation of the ocean Doppler signal, and how this effect enters into the SAR imaging theory can be found in [13].

It is thus important to be able to know very precisely the local wind and the sea state, and also to have a correct description of the ocean statistics and a proper backscattering model. The dependency of the DCA on the imaging geometry, polarization, wind field and sea state is shown in Figure 1 [13]. It is here worth noticing that the DCA is not only dependent on the wind vector, but also on the sea state, here parameterized with the wave age. The semi-empirical DCA models like CDOP [2] has no explicit dependency on the wave age. It is thus questionable of its applicability in coastal area where limited fetch is to be expected.

a)

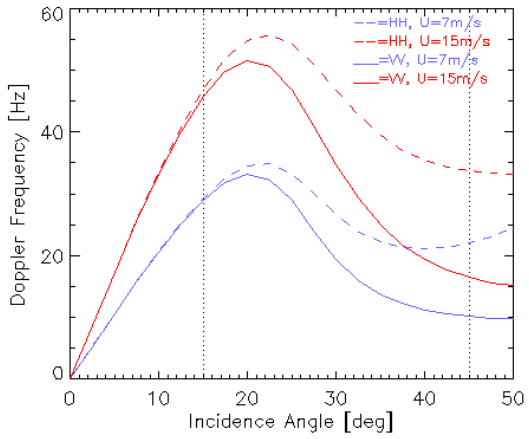

Figure 1 *: a) DCA as function of incidence angle for wind speed 15 m/s (red) and 7 m/s (blue). b) DCA as function of wind direction relative to range at an incidence angle of 20 degrees and wind speed of 12 m/s. c) DCA as function of wind speed at an incidence angle of 20 degrees and wind direction of 180 degrees relative to range. The error bars in the mid and right plots show the variability of the DCA as function of 10% change in wave age. The dotted lines are for HH and full lines for VV polarization.*

b)

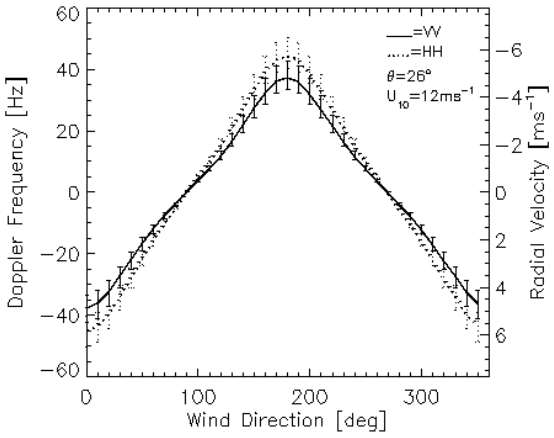

c)

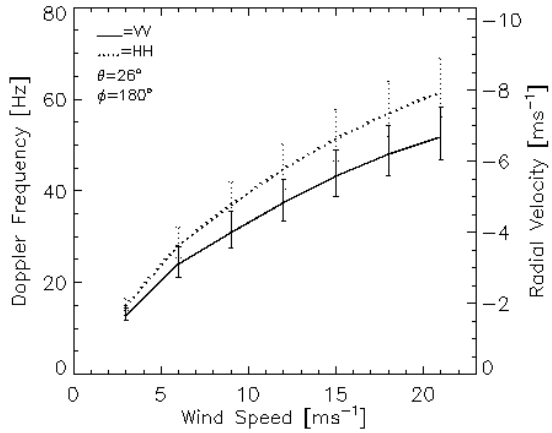

The main challenges from an ocean surface current (OSC) inversion point of view is to have a GMF that describes all the geophysical processes that contributes to the DCA equally well over a large range of incidence angles and for different polarizations. At present no such model exist. Furthermore, for application to S1+CS a similar DCA model for bi-static backscattering is needed.

1.2. S1+CS Measurable

The S1+CS constellation must be able to address both the ocean wind and wave field in addition to the surface current field. The radar observables from which these parameter usually are retrieved from are:

- Normalized radar cross section - NRCS
- Doppler anomaly - DCA
- Radar image spectra - SPC

In the S1+CS case the parameters must be estimated in both mono-static and the bi-static geometry. The SPC is the co- or cross-spectra estimated from the complex images. In addition there are also other observables that are used to retrieve wind and wave information such as wind streaks [20],[21],[22], and higher order statistical parameters derived from the images [22]. The two main processing steps of a retrieval algorithm are:

- The *parameter estimation* module
- The *geophysical retrieval* module

In the following is given a high level description of these modules of the wind/wave/current retrieval algorithm applicable for the S1+CS constellation. We include the wave imaging, although it is not currently used in any DCA based surface current retrieval schemes. However, future mission concepts, like the SKIM proposal for the EE9 addresses the measurements of wave spectra as a key component to resolve the wave induced biases measured by the DCA method, and thus achieve a better estimate of the total surface current.

2. Outline of Parameter Estimation

This section describes the high-level procedures for estimation of Doppler anomaly frequency (DCA), normalized radar cross-section (NRCS) and ocean image cross-spectra for both S1 and CS measurements. We include the image cross-spectra for the purpose of future algorithms.

The selected geometry of the S1+CS stereo constellation is shown in Figure 2 adapted from [31]. The bi-static Doppler is here defined as the rate of change of bi-static ranges, $R_{s1}+R_{cs1}$ or $R_{s1}+R_{cs2}$ along the bi-static line of sight, $\underline{\hat{e}}_{cs1}$ or $\underline{\hat{e}}_{cs2}$. The bi-static lines of sight are selected orthogonal to each other and ±45 degrees with respect to S1 line of sight in nearest swath.

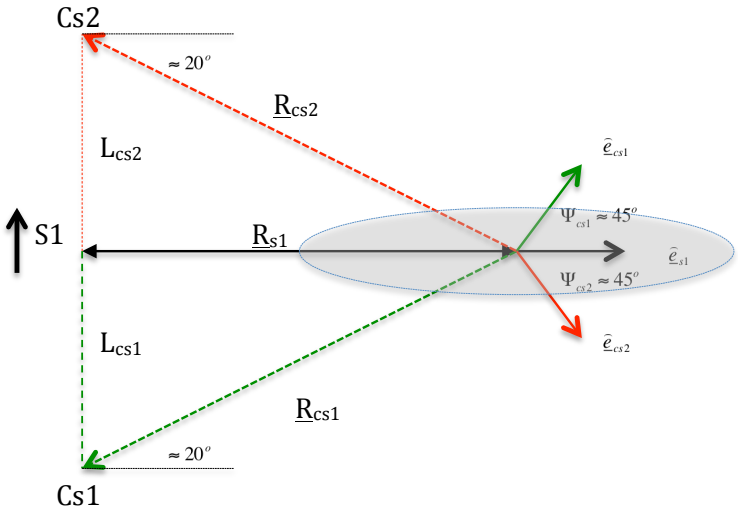

Figure 2 *: S1+CS bi-static imaging geometry. The shaded area illustrates the common area on ground illuminated by the S1 and CS antennas.*

2.1. Doppler Anomaly

The Doppler anomaly measures the range (or bi-static range in case of CS) component of the velocity of the scattering facet on the ocean surface. In the mono-static case the velocity of the scattering facet is highly correlated with the local wind speed (wave orbital motion) and the underlying surface current. However, these two contributions are not easily separated from the measured Doppler. Further discussion of this topic is given in Section 3. In the bi-static case the relation between the SAR Doppler anomaly and the motion of the underlying surface is less known, and an appropriate model needs to be established.

The Doppler centroid estimation algorithm implemented is based on using single look complex (SLC) data [5],[6], similar to the method described in [26], but extended to correct the azimuth spectra for energy aliased from neighboring areas (side-band effects). The high-precision Doppler frequency is thus estimated from a full-bandwidth processed SLC image with no windowing applied to the data

enabling the correction of sideband errors.
The algorithm models the expectation value of the azimuth spectra in terms of covariance coefficients over range of frequency bands taking into account the antenna coefficients, the true intensity and the white noise (thermal and quantization) contribution. The first order coefficient of the model is solved simultaneously with respect to phase providing an estimate of Doppler offset, and to envelope providing an estimate of the unbiased (noise corrected) intensity. The model is also used to calculate the standard deviation of the Doppler estimate. The model of the azimuth spectrum of the complex image is given in Eq.(1).

$$P(\varpi;\mathbf{t}) = \sum_j \bar{I}(\mathbf{t}-\Delta\mathbf{t}_j) D^{(j)}\left(\varpi - \varpi_{dc}(\mathbf{t}-\Delta\mathbf{t}_j)\right) + b(\mathbf{t}) \quad (1)$$

Here $\bar{I}$ is the average target intensity inside the estimation area, ϖ_{dc} is the Doppler frequency, b(**t**) is the additive noise, and $D^{(j)}$ are the antenna profiles for each of the *PRF*-bands (indexed by j) aliasing together. The 2D time variable **t** is the center position of the sub-area in the SLC from where the azimuth direction spectrum is estimated, and $\Delta\mathbf{t}_j$ is the 2D time offsets to the location of the different intensity contributions ($\Delta\mathbf{t}_j \equiv 0$ represent the position to the true intensity and $\Delta\mathbf{t}_j \neq 0$ represents the position to ghost image intensities). The range direction component of $\Delta\mathbf{t}_j$ is the range-migration and the azimuth component is j-times the PRF divided by the Doppler rate [27]. The corresponding first order inverse Fourier coefficients can be written as:

$$p_1(\mathbf{t}) = \sum_j f(\mathbf{t}-\Delta\mathbf{t}_j) d_1^{(j)} \quad (2)$$

where $f(\mathbf{t}) = \bar{I}(\mathbf{t}) e^{i\varpi_{dc}(\mathbf{t})\Delta\tau}$ provides estimate of the Doppler frequency, ϖ_{dc} and the true image intensity, $\bar{I}$. Inversion of Eq.(2) with respect to *f* is easily done by Fourier transforming the equation and introducing the Fourier transform $\hat{p}_1$ of p_1 with respect to the estimation position **t**, yielding:

$$f(\mathbf{t}) = \frac{1}{(2\pi)^2} \iint d\omega\, e^{i\omega\cdot\mathbf{t}} \frac{\hat{p}_1(\omega)}{\sum_j d_1^{(j)} e^{-i\omega\cdot\Delta\mathbf{t}_j}} \quad (3)$$

The algorithm provides a fast and easy way to solve for Doppler frequency and true intensity, and simultaneously correcting for errors caused by aliasing of intensity from side bands. The algorithm can be adapted to the bi-static case, but the modelling of the antenna will be different. This is will further described in the report from Task 1 of the CCN.

The estimation model can also used to calculate the standard deviation of the Doppler estimate [6]. The resolution of the grid is typical between *2* and *4 km (IW and EW, respectively)* depending on the resolution of the input SAR product.

It is important to notice that the estimated Doppler frequency consists in general of several terms:

$$\varpi_{dc} = \varpi_{dc}^{phys} + \varpi_{dc}^{geo} + \varpi_{dc}^{elec} + \Delta\varpi_{dc} \quad (4)$$

Here ϖ_{dc}^{phys} is the geophysical term, ϖ_{dc}^{geo} is the geometric term, ϖ_{dc}^{elec} is the antenna electronic miss pointing, and $\Delta\varpi_{dc}$ is a residual error coming from imperfect prediction of the non geophysical terms or other unknown biases. The interesting term is the ϖ_{dc}^{phys}, so the other terms must be predicted

carefully and remove from Eq.(4). The geometric term is computed from the orbit/attitude data as part of the Doppler estimation. The electronic miss pointing can also be computed if the antenna model is provided, as is the case for Sentinel 1. Alternatively, it can be estimated from SAR data acquired over rain forest or other homogenous areas of no motion. If there are land areas within the scene, the residual error, $\Delta\varpi_{dc}$ can be removed by setting the land area Doppler to zero after first correcting for the deterministic terms in Eq.(4). A more precise approach to estimate $\Delta\varpi_{dc}$ is using a simple two-parameter physical model in *pitch* and *yaw* [*32*].The calibration approach applied to S1A IW and EW data at present is outlined below:

- Remove the geometric and electronic miss pointing Doppler from the observed Doppler

$$\delta\varpi = \varpi_{dc} - \varpi_{dc}^{geo} - \varpi_{dc}^{elec} \quad (5)$$

- Make the residual Doppler, δϖ continuous from one swath to another by merging the Doppler values in azimuth at the swath borders
- Use land areas within the scene to absolute calibrate the residual Doppler

$$\varpi_{dc}^{phys} = \delta\varpi - \langle\delta\varpi\rangle_{LAND} \quad (6)$$

- Here $<\delta\varpi>_{LAND}$ is the mean Doppler over land areas within the swath.

In Figure 3 is shown Doppler anomaly and radial velocity estimated from Sentinel 1A over Agulhas using this approach. In b) negative range velocity means component towards the radar, and positive along radar line of sight. Here land areas are used to absolute calibrate the estimated Doppler values. In this data set we see both signature from wind/wave and surface current in the Doppler image.

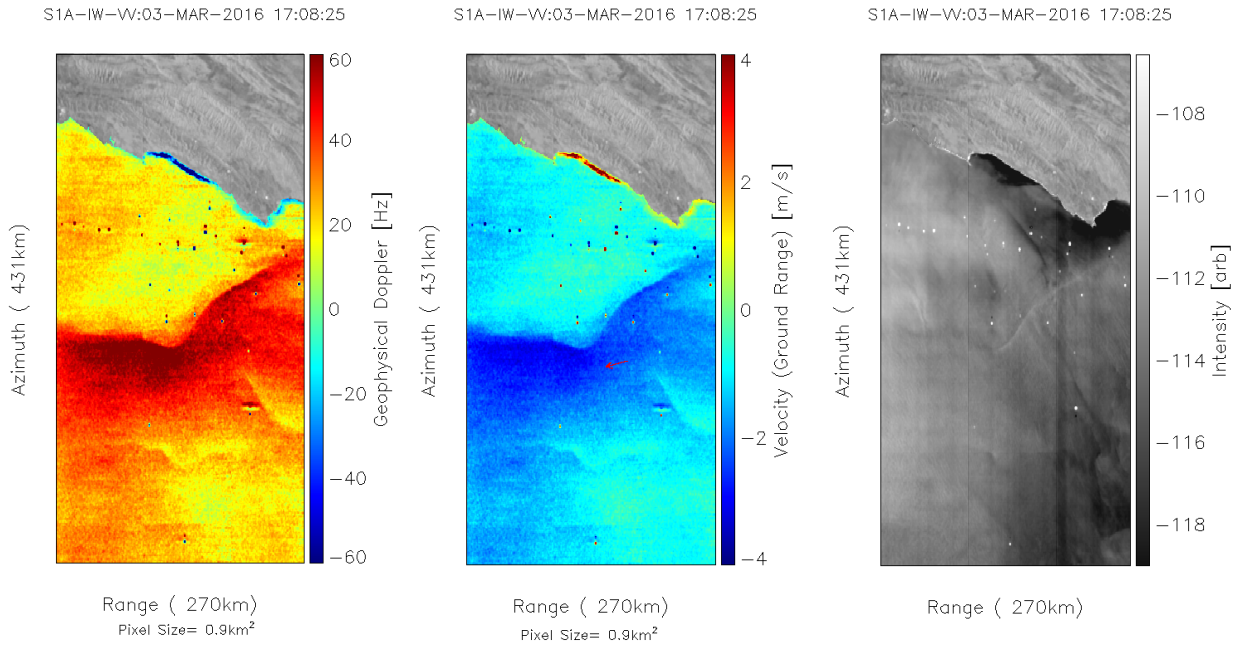

a) b) c)

Figure 3 *: a) Doppler anomaly frequency, b) radial velocity, c) Intensity image. Sentinel 1A IW mode acquired over Agulhas outside South-Africa (ascending pass). The red arrow in figure b) indicates the Lagrangian drifter location and direction. The drifter speed was measured to 1.1 m/s in the ground range direction.*

2.1.1. Requirements and Error Sources

The two main deterministic error sources to the Doppler anomaly are:

- Imperfect prediction of the attitude Doppler centroid. There is large discrepancy between the geometric Doppler computed from the quaternions within the downlinked source package currently available to the Level 2 processor, and the DC estimated from land data as shown in Figure 4 for Sentinel 1B and Figure 5 for Sentinel 1A. This causes latitude variations (high order harmonic oscillation with up to ±20Hz in amplitude for S1B) in the estimated Doppler anomaly. This attitude DC oscillations are also observed to drift with time, significantly over a few days.
- Imperfect prediction of Doppler centroid bias from antenna. This causes a bias in Doppler anomaly as function of elevation angle.

The attitude problem has been the major obstacle for utilizing the Sentinel 1A Doppler products, especially the WV mode since no land is available in the vicinity of the images. However, for Sentinel 1B improvements in attitude control has improved significantly the DCA data, but still insufficient for reaching the required DCA accuracy. Recent global ocean data from S1B WV shows better correlation (0.86 in swath *wv1*, 0.78 in swath *wv2*) between DCA and range wind speed than for S1A, as shown in Figure 6. The spread in DCA observed in Figure 6 for a given wind speed is a combination of geophysical variability (wave age, current), error in the model wind field, and a residue signal from the geometric Doppler. The latter is the dominant contribution.

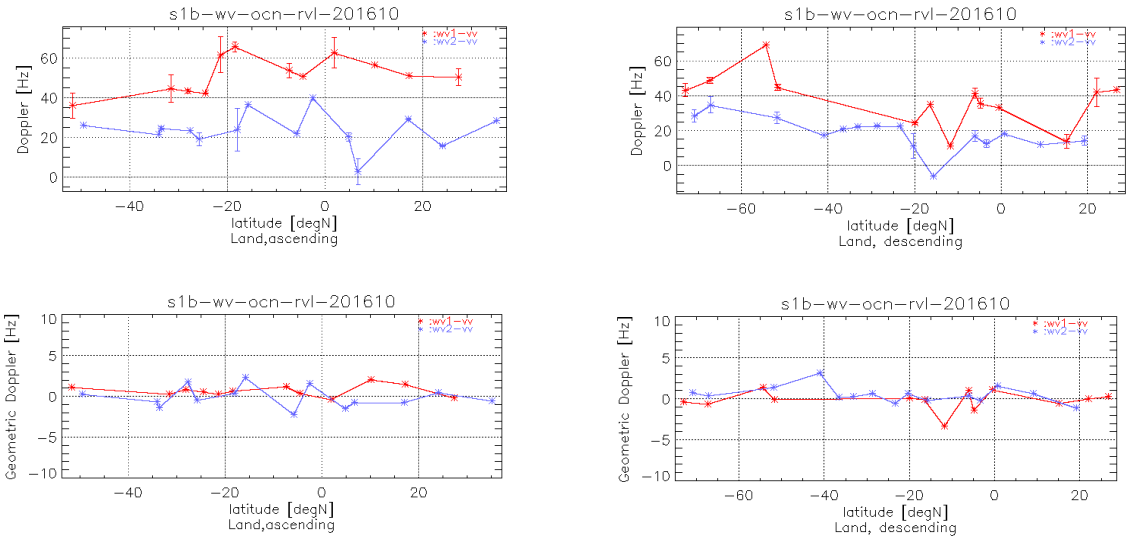

Figure 4 *: Sentinel 1B WV Doppler centroid estimated from data over land (upper plots), and the corresponding geometric Doppler (lower) computed from orbit and attitude (quaternions) data. Left plots are from ascending and right plots from descending tracks. Data acquired during October 2016.*

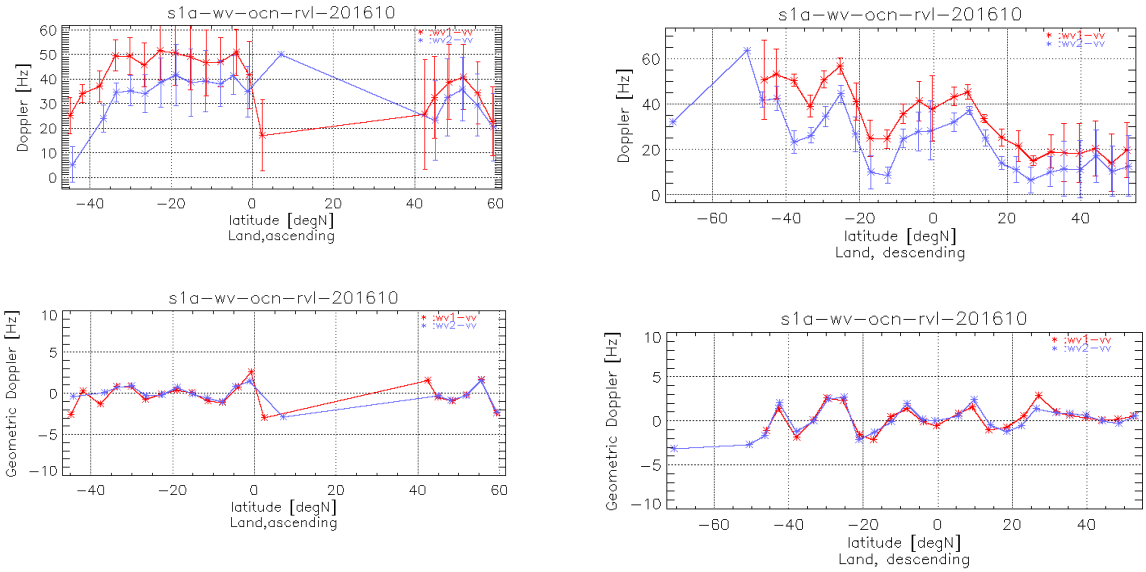

Figure 5 *: Sentinel 1A WV Doppler centroid estimated from data over land (upper plots), and the corresponding geometric Doppler (lower) computed from orbit and attitude (quaternions) data. Left plots are from ascending and right plots from descending tracks. Data acquired during October 2016.*

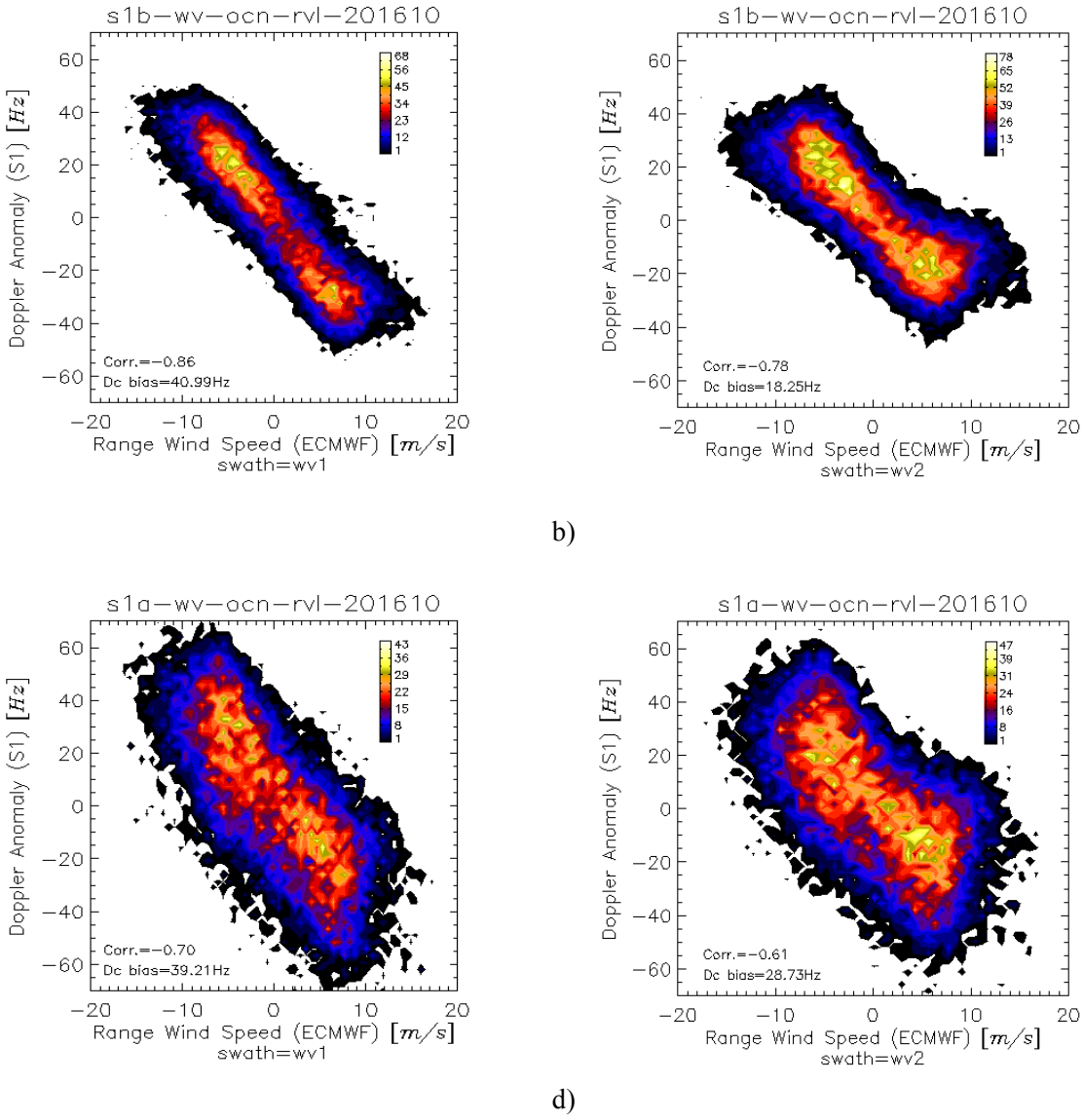

Figure 6 *: Sentinel 1B and 1A Doppler anomaly versus ECMWF wind speed along range direction acquired in swaths wv1 (a,c) and wv2 (b,d). Data acquired globally from 1st to 31st October 2016. The DC biases indicated in the plots are removed from the Doppler anomaly before plotting the data.*

The next critical factor for DCA accuracy is the DC bias from antenna over the swaths. In Figure 7 is shown current status of the prediction of Dc bias from antenna electronic miss-pointing versus observation over rainforest. We note that the prediction is quite good ($\leq \pm 2$Hz) except for the nearest swaths i.e. IW1 and EW1. We also see some small jumps between swaths that are not perfectly predicted by the model. However, these biases can easily be removed by processing the Dc with a little overlap between swaths, and forcing continuation of DCA over swaths as described in Section 2.1.

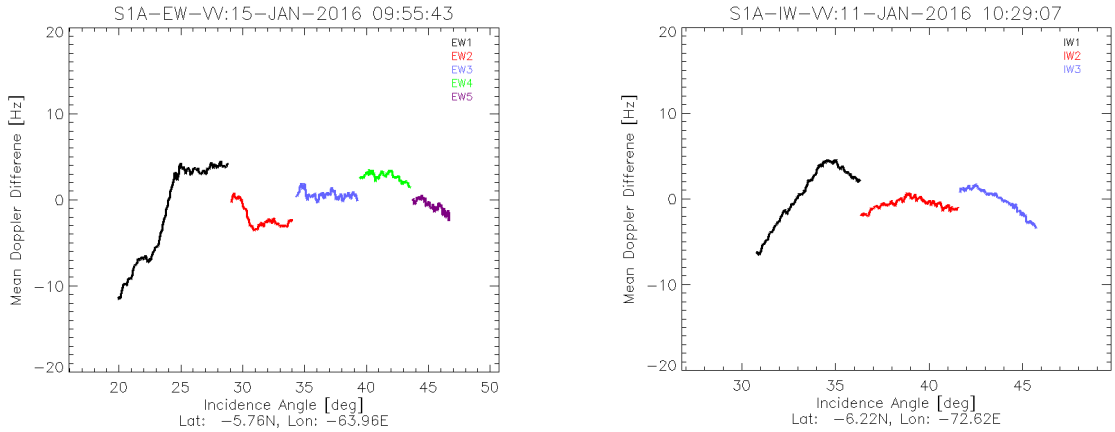

a) b)

Figure 7 *: Mean Doppler difference (Dc data – Dc antenna) as function of incidence angle for Sentinel 1A EW (a) and IW (b) modes. Data acquired over rain forest. Dc antenna computed from antenna model.*

In addition there are several statistical errors sources:

- Scene inhomogeneity. Any inhomogeneity within the estimation area will increase the standard deviation of the estimated Doppler centroid.
- Signal-to-noise ratio. Reduced signal-to-noise ratio will increase the uncertainty of the Doppler centroid estimate.
- Aliasing from side band. The correction of aliasing from side band is not perfect. The residue side band aliasing will increase the Doppler estimate. The relation between pulse repetition frequency and antenna length in azimuth controls the amount of side band aliasing. For Sentinel 1 this factor will varies with swath, and the best swaths are IW1, IW3, EW2 and EW4.

The impact of side band correction on the Doppler centroid estimate is shown in Figure 9 for a typical ocean scene with inhomogeneity and slick area. We observe that side band correction is particular important in areas with low signal-to-noise ratio.

Although the statistical errors mentioned above can cause large (10s of Hz) variance in the DCA estimate, they can be predicted and thus used to flag the data. An example of this from Sentinel 1A is shown in Figure 8. We see that the low wind areas (black areas) in the intensity image c) causes unrealistic and noisy Doppler values a), but also very high values for the predicted Doppler standard deviation b). It is thus important that the Doppler estimators for the both S1 and CS also provide a good prediction of the Doppler standard deviation on the same grid as the Doppler anomaly.

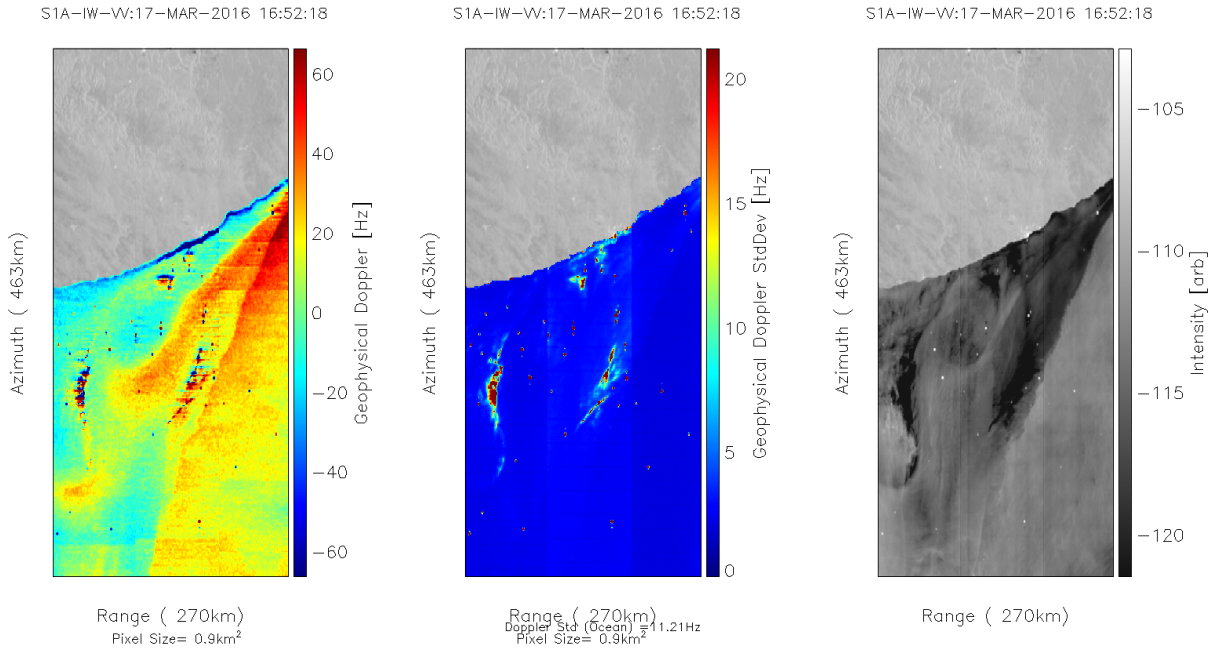

a) b) c)

Figure 8 *: a) Doppler anomaly, b) Predicted Doppler anomaly standard deviation, c)Image intensity. Data from Sentinel 1A IW mode over Agulhas.*

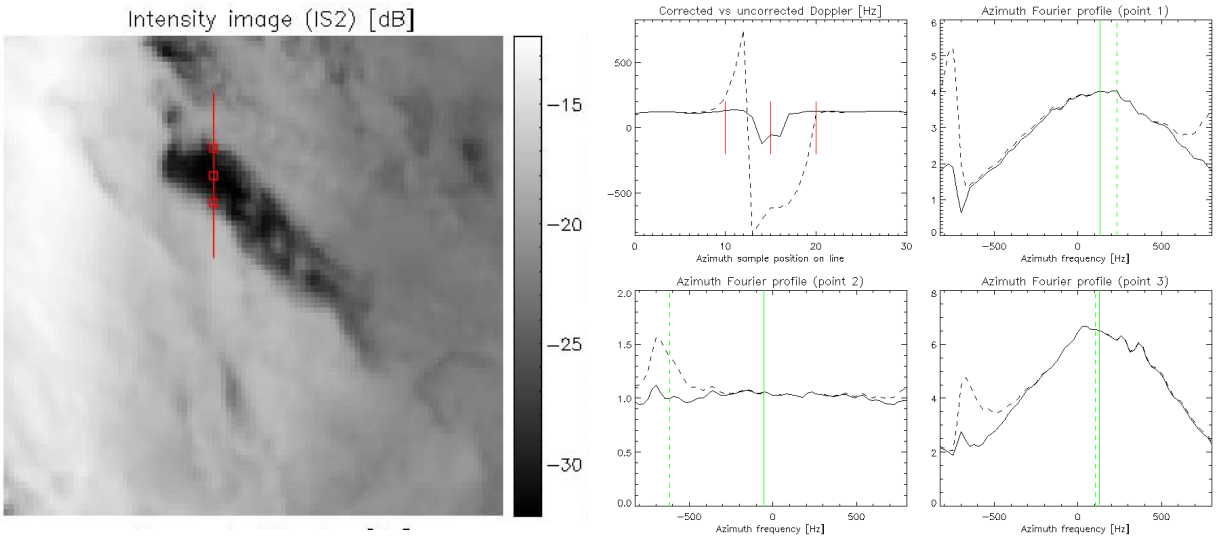

a) b)

Figure 9 *: a) Image intensity of an ocean slick area. b) Azimuth Doppler centroid profiles along the red line in a) uncorrected (---) and corrected (__) for side band aliasing. Azimuth Fourier profiles from the red squares in a) without (---) and with (__) side band correction. The green lines indicate the estimated Doppler centroid with without (---) and without (__) side band correction.*

2.1.2. Doppler analysis of Sentinel 1b

Recently, a data driven approach has been developed for the high-bandwidth Sentinel 1 data to reconstruct the Doppler anomaly using massive global S1b WV data sets. The method provides an estimate of both the geophysical Doppler and the total geometric Doppler. The total geometric Doppler is the sum of the attitude Doppler and the electronic (EM) miss pointing Doppler. The performance of the DC models has been validated both using ocean and land data. A scatterplot of the basic performance is shown in Figure 10. Over land areas a standard deviation of only 3Hz is achieved.

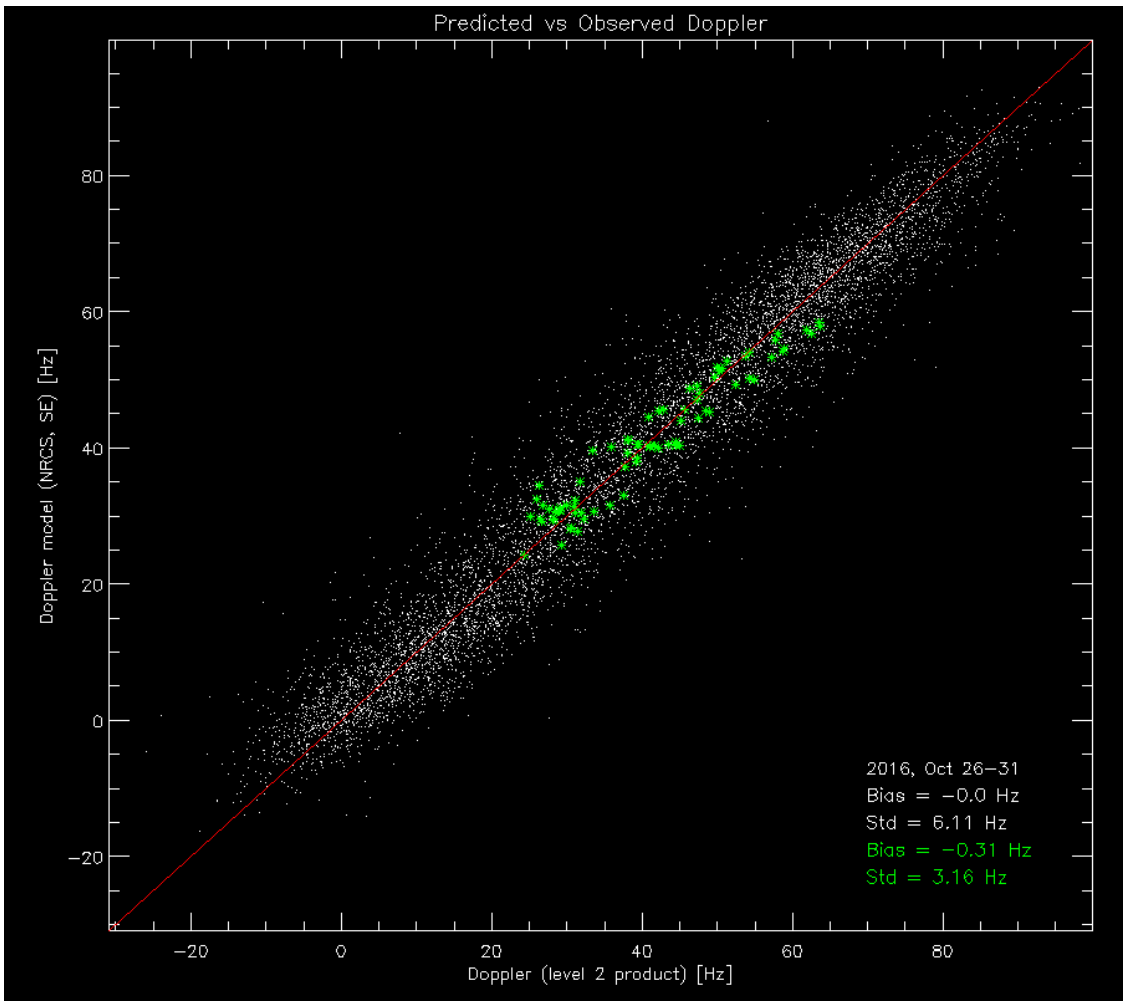

Figure 10 *: Scatterplot of total DC model versus measured DC from the period of 26-31 October 2016 from S1b acquired in WV1. The green dots are data acquired over land areas.*

The geometric Doppler has been compared with the recent attitude Doppler computed independently by ESA from restituted attitude data. In Figure 11 is shown the geometric Doppler for S1b WV1 orbits for 28 October 2016 together with the computed attitude Doppler.

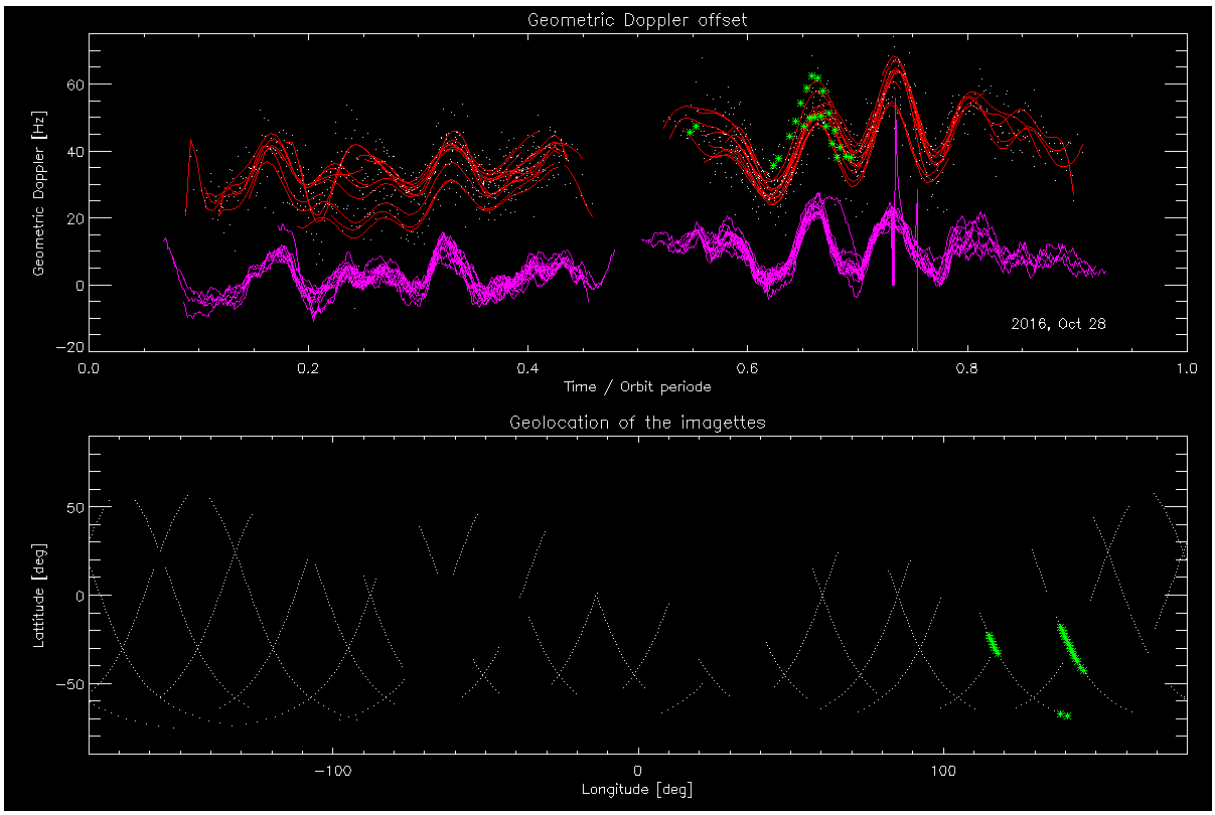

Figure 11 *: Upper: Geometric Doppler computed from data (red) and from restituted attitude data (pink) for 28 October 2016 for Sentinel 1b WV1. Lower: Location of tracks. The green points are data acquired over land areas.*

The conclusion so far is that the attitude Doppler computed from quaternions predicts well the main variations of the Doppler around the orbit. However, the spread of the data driven geometric Doppler is significantly larger, which cannot be explained by geophysical Doppler model limitations, nor the EM Dc bias. The mean offset of the curves in Figure 11 is in agreement with the EM Doppler bias computed from antenna model.

There is also some noise in the computed attitude Doppler that needs to be removed in order to put it directly into the Level 1 processing chain. One strategy for future calibration and monitoring of the Doppler can be a combined use of computed attitude Doppler from quaternions and a data driven estimate of the residual geometric Doppler variations. This will simplify and improve the data driven approach since most of the oscillations in the geometric Doppler is removed by the attitude Doppler computed from the quaternions.

The WV mode of Sentinel 1 can then be used systematically to monitor and calibrate the Doppler anomaly and provide DC calibration data on orbit level covering all latitudes. The preliminary results show that a DC accuracy of around 2-3 Hz is feasible.

2.2. NRCS

NRCS can easily be estimated from the SLC data by up-sampling, detection and spatial averaging (re-sampling) (< >) followed by a conversion to ground range and absolute calibration:

$$\sigma_o(\theta) = C \cdot \left(\left\langle |I_c|^2 \right\rangle - N(\theta) \right) \cdot \sin\theta \tag{7}$$

Here θ is local incidence angle, I_c is the complex pixel from the SLC, N is the additive noise intensity, and C is the absolute calibration constant. Usually the SAR processors are well calibrated which means that C= 1 in Eq.(7). The NRCS can usually be estimated on a grid down to a resolution of 0.*5km* depending on the resolution of the input SAR product. Note that the additive noise in in general dependent on the incidence angle and polarization, and must estimated separately or provided within the product (*de-noising vector*). This is especially critical in wide swath imaging such as the S-1 IW and EW modes.

There are no specific differences in estimating the NRCS from mono- and bi-static measurements, assuming both SLC area calibrated.

2.2.1. Requirements and Error Sources

The main error source to estimation of the NRCS comes from imperfect compensation for the additive noise. A noise correction profile is usually provided within the product, but the profile can also be established from massive data.

The estimation and correction of additive noise is especially important for cross-pol data because of low ocean backscatter in cross polarization.

2.3. Image Cross-Spectra

The estimation of image cross-spectra, P_s is different for SM/WV data and TOPS data. The sweeping of the antenna in TOPS Mode reduces effectively the achievable inter look separation time and thus the ability to get a good ambiguity free estimation of the wave direction. However, the burst and swath overlap areas in TOPS mode can be exploited for ambiguity free wave spectral retrievals.

In case of TOPS data, inter-looking is not necessary since there exist two looks in the burst overlap areas. The cross-spectra, P_s can be directly generated from the neighboring burst overlap zone as given by Eq.(8).

$$P_s^{(m,m+1)}\left(\underline{k},\tau\right) = \frac{1}{\left\langle I^{(m)}\right\rangle\left\langle I^{(m+1)}\right\rangle}\left\langle I^{(m)}\left(\underline{k},0\right)I^{(m+1)^*}\left(\underline{k},\tau\right)\right\rangle - \delta\left(\underline{k}\right) \tag{8}$$

where $\langle I^m \rangle$ is the mean intensity, and $I^{(m)}(\underline{k},\tau)$ is the Fourier transform of the overlap intensity image of burst m. Here, τ denotes the effective look separation time given as the time delay between burst m and $m+1$. However, the noise of the TOPS cross-spectra is relatively high because the overlapping area is much smaller than the burst length (≈3km), but the look separation time is large ($\tau \approx 2.5$ sec) resulting in a large phase shift of the cross-spectra caused by the imaged waves. Note that for SM/WV mode the typical look separation time is only around 0.4 sec. Example of cross spectra from S1A IW mode is shown in Figure 12.

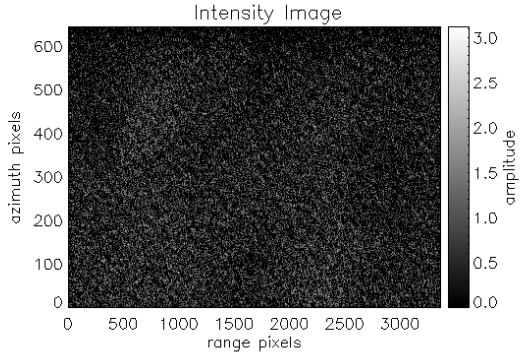

a)

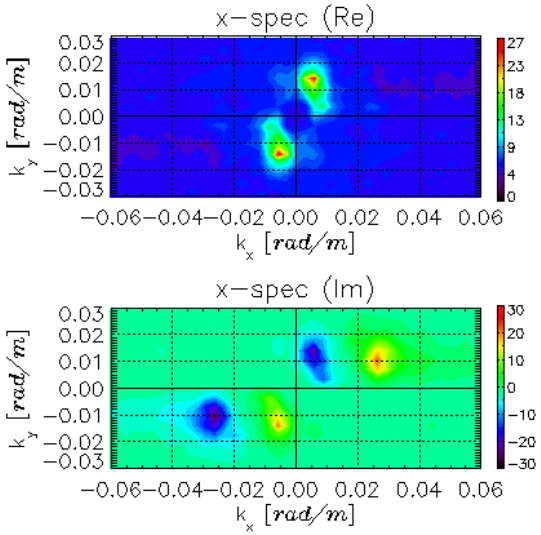

b)

Figure 12 *: a) Intensity image from burst overlap area, b) image cross-spectra between burst overlap images (real and imaginary part). A bi-modal wave system is observed, with opposite propagating swell and wind sea spectra.*

Note from Figure 12 that the imaginary part of the cross-spectra is as strong as the real part. This is due to the large look separation time achieved from Sentinel 1A IW or EW TOPS data.

The SAR derived wave spectra only provide good spectral information of the swell part of the spectra. Research is on going to extract wave age from the SAR image spectra. A first approach is implemented in the S1 WV and SM Level 2 processor.

2.3.1. Requirements and Error Sources

The main error sources to the estimation of wave parameters are the prediction of the modulation transfer function. At present an accuracy of around 0.4 m is achieved for the significant wave height for waves resolved by the SAR [9]. This is also the accuracy of the total significant wave height derived from empirical statistical based algorithms [22]. No validation of the wave age estimation exists.

3. Outline of Inversion Module

A surface current inversion algorithm needs ideally to be based on a coupled wind/wave/current retrieval approach since knowledge of the sea-state and the wind vector are needed for retrieval of the surface current component. Such an approach is still a research topic. The usual approach is to neglect the sea state information (i.e. wave age) and perform the retrieval by combining the DCA and the NRCS using CDOP and CMOD (or similar GMFs) together with external model wind field, either in a direct or in a Bayesian approach. For single-pol data in a mono-static configuration, use of independent information on wind direction is always required. For the stereo SAR concept the retrieval of the wind vector can be feasible by combining NRCS from both the S1 and the CS. However, the accuracy of the bi-static scattering model needs to be assessed, and GMFs need to be established for the bi-static case. It should also be emphasized that applying CMOD type of GMF in strong current areas will give large errors in the SAR derived wind field, and thus also in the surface current field.
The concepts of the GMFs are briefly described in the following.

3.1. Geophysical Model Functions

For C-band SAR the wave induced Doppler and the NRCS can be predicted by use of semi-emphirical GMFs such as the CDOP, CMOD or C-SARMOD for the mono-static case, respectively. However, for bi-static measurements no GMF such as CDOP, CMOD or C-SARMOD exist. An alternative approach is to use pure physical based models such as the [1], [2],[8],[11],[12],[13],[14],[29]. However, it is worth mentioning that the pure physical based models are very sensitive to the physical description and statistical properties of the ocean surface used in the model [28].

For bi-static case pure physical models, such as the SSA model used in [31], are at present the only alternative for the describing the NRCS and the DCA. However, they are quite computer intensive, not easy to use in an operational context and also dependent on the physical description and statistical properties of the ocean surface. Another critical comments to these models are that they do not include effects of breaking waves. Extending the model by adding a breaking term is needed.

The Doppler model in [13] can easily be extended to the bi-static backscattering case.

In any case, the general interface to the GMFs can be formulated as:

$$GMF = F\left(\phi, U_{10}, \gamma, u_r, \theta_i, \theta_s, pol\right) \tag{9}$$

where

- ϕ = wind direction relative to range [*deg*]
- U_{10} = wind speed [*m/s*]
- γ = wave age [*norm*]
- u_r = surface current - ground range component [*m/s*]
- θ_i = local radar beam incidence angle [*deg*]
- θ_s = local bi-static scattering angle [*deg*]
- pol = radar polarization (*vv*, *hh, hv,vh*)

Here *GMF* can represent the Doppler anomaly $\left(\varpi_{sx}^{phya}\right)$, the NRCS (σ_o), and the image cross-spectra (P_k)

3.1.1. Normalized Radar Cross Section

The co-polarization GMF for the NRCS is usually provided as a harmonic decomposition in relative wind direction:

$$\sigma_o(\theta,U_{10},\phi) = a_o(\theta,U_{10})\cdot\left[1 + a_1(\theta,U_{10})\cos\phi + a_2(\theta,U_{10})\cos 2\phi\right] \quad (10)$$

Specific values for the coefficient, a_0,a_1,a_2 are derived for C-band SAR observations (C-SARMOD), and recent values and performance using Sentinel 1A and Radarsat 2 data can be found in [24]. The coefficients in Eq.(10) are derived for both *vv* and *hh* polarization.

For cross-polarization a simple empirical relationships are proposed by Vachon and Wolfe [2011] for Quad-pol RS-2 data and by Hwang et al. [2015] and Zhang et al. [2014] for RS-2 dual-pol data:

$$\sigma_o^{x-pol}(\theta,U_{10}) = \alpha\cdot U_{10} + \beta \quad (11)$$

Here α,β are empirical fitted constants. Note that the cross-pol GMF has no wind direction dependency. A systematic comparison between observation of cross-pol NRCS versus wind speed derived from different C-band missions (including S1A) and different empirical models can be found in [24]. A typical wind field dependency of the NRCS GMFs is shown in Figure 13.

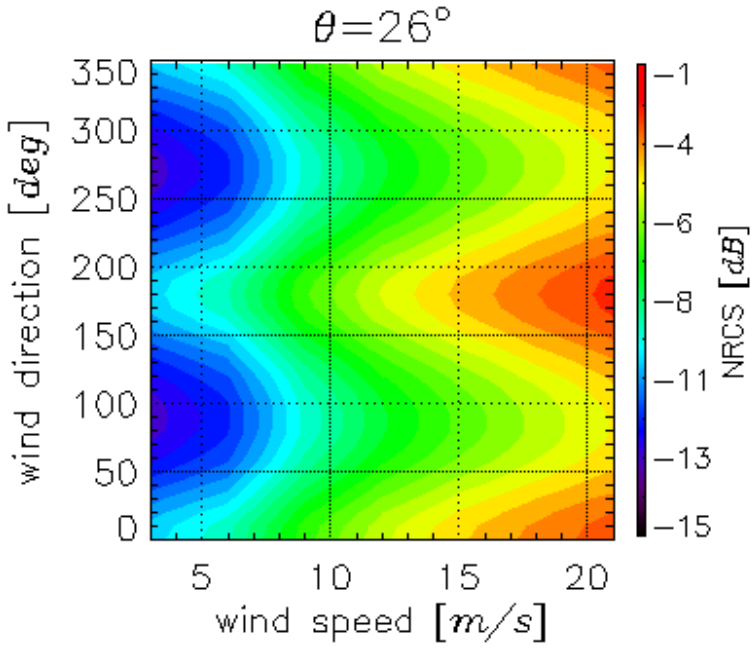

Figure 13 *: NRCS at c-band and vv-polarization. Incidence angle indicated in the figure. The wind direction is relative to azimuth, with 0 deg corresponding to upwind, and 90 deg cross wind.*

3.1.2. Doppler Anomaly

At this stage we do not attempt to include the wave/current interaction processes in the Doppler anomaly model, although such models do exist [29], [30]. In our approximation, the surface current contribution in the GCM-Dop model is thus just an underlying drift of the surface added to the wind/wave contribution such as:

$$\begin{aligned} \varpi_{dc}^{phys} &= \varpi_{dc}^{phys}\left(\phi, U_{10}, \gamma, u_r, \theta, pol\right) \\ &\approx -2k_{rad}u_r + \varpi_{dc}^{phys}\left(\phi, U_{10}, \gamma, \theta, pol\right) \end{aligned} \tag{12}$$

Here the term $-2k_{rad}u_r$ is the Doppler shift from a steady current, which in general is a mixture of Ekman, tidal and geostrophic currents. We thus write our GMF for the DCA measurements as a sum of a GMF for the surface current plus GMF for the wind/wave induced drift:

$$\varpi_{dc}^{phys} = \varpi_{dc}^{cur} + \varpi_{dc}^{wave} \tag{13}$$

The semi-empirical Doppler anomaly model describing the wind/wave contribution is parameterized as [2]:

$$\varpi_{dc}^{c\,\mathrm{mod}} = CDOP\left(\phi, U_{10}, \theta, pol\right) \tag{14}$$

The coefficients of Eq.(14) are derived fro both *vv* and *hh* polarization. It is the fastest and easiest model to use for describing the ϖ_{dc}^{wave} term in Eq.(13). However, it should be emphasized that the performance depends on the imaging geometry, and only applicable for co-polarization. For application on S-1 TOPS data the performance will thus vary with swath. A typical wind field dependency of the Doppler anomaly GMFs is shown in Figure 14:

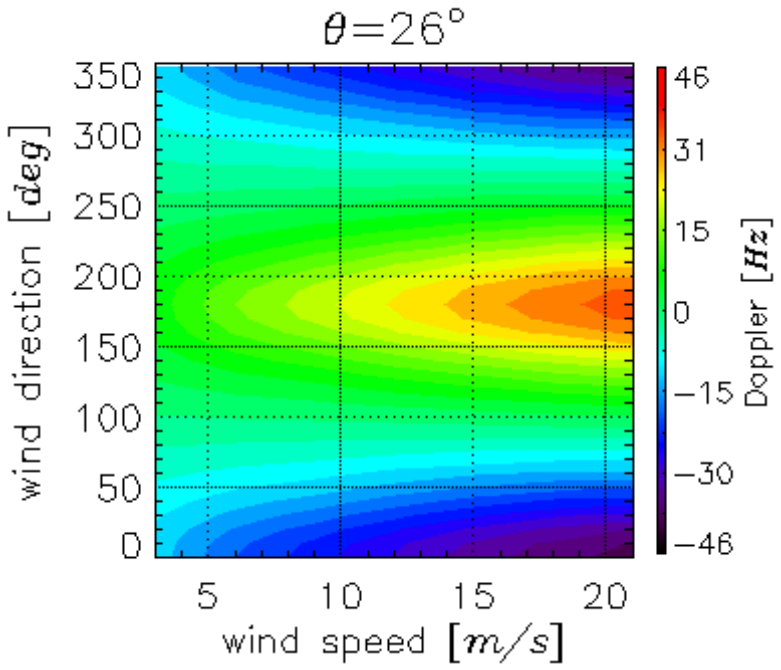

Figure 14 *: Doppler anomaly at c-band and vv-polarization. Incidence angle indicated in the figure. The wind direction is relative to azimuth, with 0 deg corresponding to upwind, and 90 deg cross wind.*

3.1.3. Image Spectra

The GMF for the image spectra is the ocean-to-SAR cross-spectral transform [7], which is an integral transform of a product between a exponential term and a polynomial term. However, in the operaitonal use this integral transform is splitted into a sum of a quasi-linear and a non-linear term (P_{nlin}) as follow:

$$\begin{aligned} P(\underline{k},t) &= P_{qlin}(\underline{k},t) + P_{nlin}(\underline{k},t) \\ &= \frac{1}{2} e^{-\left(k_y \lambda_c / 2\pi\right)^2} \left\{ \left|T(\underline{k})\right|^2 e^{-i\omega_{|\underline{k}|}t} S(\underline{k}) + \left|T(-\underline{k})\right|^2 e^{i\omega_{|\underline{k}|}t} S(-\underline{k}) \right\} + P_{nlin}\left(\underline{k},t\right)\Big|_{S(\underline{k})} \end{aligned} \quad (15)$$

Here $\underline{k} = (k_x, k_y)$ (range, azimuth) is the wave vector, t is the look separation time, λ_c is azimuth cut-off wavelength [m], T is the total modulation transfer function, $\omega_{|\underline{k}|}$ is wave dispersion relation, and $S(\underline{k})$ is the underlying ocean wave spectra. In Figure 15 is shown the output of the different terms of the forward integral transform given in Eq.(15) for a given input ocean wave spectrum.

Research is undertaken to retrieve information on the total sea state, including wave age, from the SAR spectra.

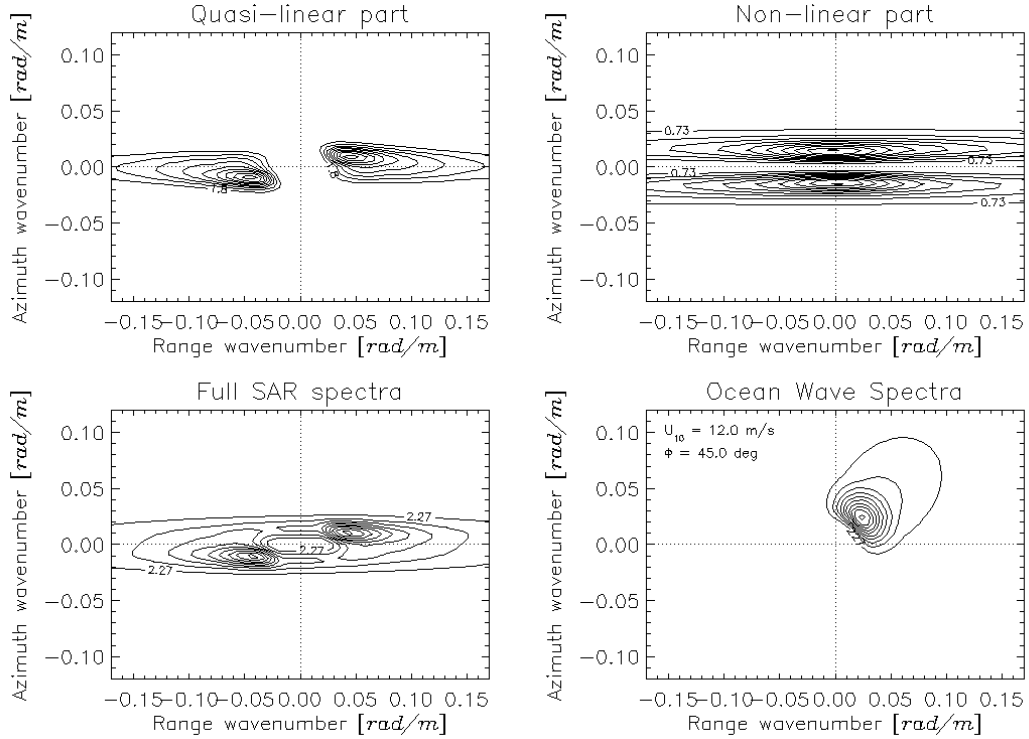

Figure 15 *: Upper left: Quasi-linear SAR image spectra,* $|P_{qlin}(\underline{k})|$. *Upper right: Non-linear SAR image spectra,* $|P_{nlin}(\underline{k})|$. *Lower left: Total SAR image spectra,* $|P(\underline{k})|$. *Lower right: Ocean wave spectra,* $S(\underline{k})$

3.2. Inversion Models

The goal of the inversion is to extract the surface current. We describe here the state-of-the approach used for mono-static DCA measurements, and extend it to take into account also the bi-static measurements. This is a direct approach where we first solve for the wind field and then use the wind field to solve for the surface current. The wind and surface current field retrieval is based on using the measured NRCS and the Doppler anomaly in combination with the corresponding GMFs and the model wind field, $\underline{U}_{10}^{\mathrm{mod}}$ (from numerical atmospheric model) in a Bayesian approach.

First, the retrieval of the wind field, $\underline{U}_{10}$ is done by minimizing the following cost function [8]:

$$J\left(\underline{U}_{10}\right)=\sum_{j\in\{s1,cs1,cs2\}}\frac{\left(\sigma_{o-\mathrm{mod}}^{(j)}\left(\underline{U}_{10}\right)-\sigma_{o-obs}^{(j)}\right)^2}{Var\left(\sigma_{o-obs}^{(j)}\right)}+\frac{\left(\varpi_{dc-\mathrm{mod}}^{wave,(j)}\left(\underline{U}_{10}\right)-\varpi_{dc-obs}^{phys,(j)}\right)^2}{Var\left(\varpi_{dc-obs}^{phys,(j)}\right)}+\frac{\left(\underline{U}_{10}-\underline{U}_{10}^{\mathrm{mod}}\right)^2}{Var\left(\underline{U}_{10}^{\mathrm{mod}}\right)} \tag{16}$$

Here the summation *j* is over the S1 and the Cs measurements, and the subscript *mod* means the predicted GMF values and *obs* means the corresponding value estimated from the SAR data. The *Var* means the variance. The use of the DCA measurements in the cost function will restrict the solution space for the wind field, but still external ambiguity wind information is needed such as from numerical wave model as indicated by the last term in Eq.(16). This will by construction provide only one solution.

The solution of Eq. (16) for the wind vector $\underline{U}_{10}$ can now be fed into the Doppler GMF of Eq.(14), and the radial surface current is derived from the difference between the measured and the predicted Doppler frequency, individually computed for the S1 and the Cs geometries:

$$U_r^{(j)}=-\frac{c\cdot\left(\varpi_{dc-obs}^{phys,(j)}-\varpi_{dc-\mathrm{mod}}^{wave,(j)}\left(\underline{U}_{10}\right)\right)}{2f_{rad}}\qquad j\in\{s1,cs1,cs2\} \tag{17}$$

Here c is the speed of light and f_{rad} is the radar frequency. The total surface current vector in the azimuth, ground range plane $(\hat{x},\hat{y})$ can then established by combining the radial components, $U_r^{(j)}$ from mono-static and bi-static geometries. The surface current direction ϕ relative to S1 range is computed as (see Figure 16):

$$\phi=\tan^{-1}\left(\frac{U_r^{cs1}-U_r^{cs2}}{2U_r^{s1}\sin\psi_{cs}}\right) \tag{18}$$

The S1+CS derived surface current vector, $\underline{U}$ in the in $(\underline{\hat{x}},\underline{\hat{y}})$ -plane can then be written as:

$$\underline{U}=U_r^{s1}\,\underline{\hat{x}}+U_r^{s1}\tan\phi\cdot\underline{\hat{y}} \tag{19}$$

Here ϕ is the surface current direction relative to S1 radar line of sight and $|\underline{U}|$ is the surface current speed. Here $\psi_{cs}=\psi_{cs1}=-\psi_{cs2}$ are the angle between the s1 plane of incidence and the bisector planes of cs1 and cs2. And $\theta_{s1},\theta_{cs1},\theta_{cs2}$ are the incidence angles of S1 (i.e. in the plane of incidence) and of the Cs1and Cs2 (i.e. in the bisector planes), respectively. The relation between the S1+CS radial surface current components and the total surface current vector is illustrated in Figure 16. A schematic flowchart of the retrieval approach outlined above is shown in Figure 17.

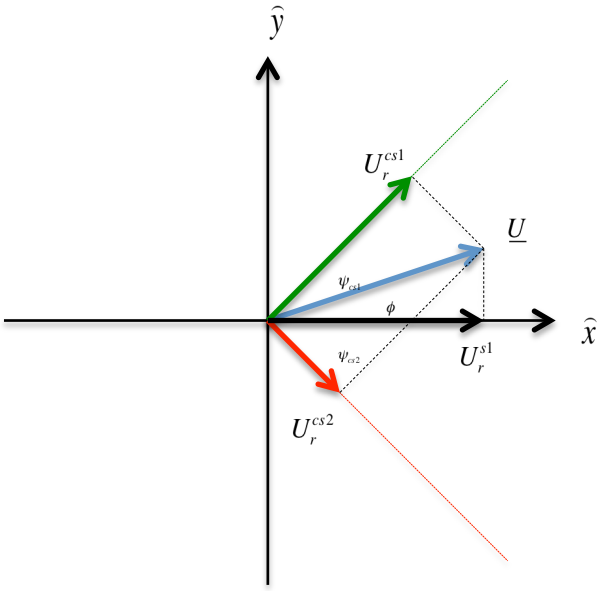

Figure 16 *: Relation between the radial surface current vector components of S1+CS and the total surface current vector $\underline{U}$ at an angle of ϕ with respect to S1 ground range.*

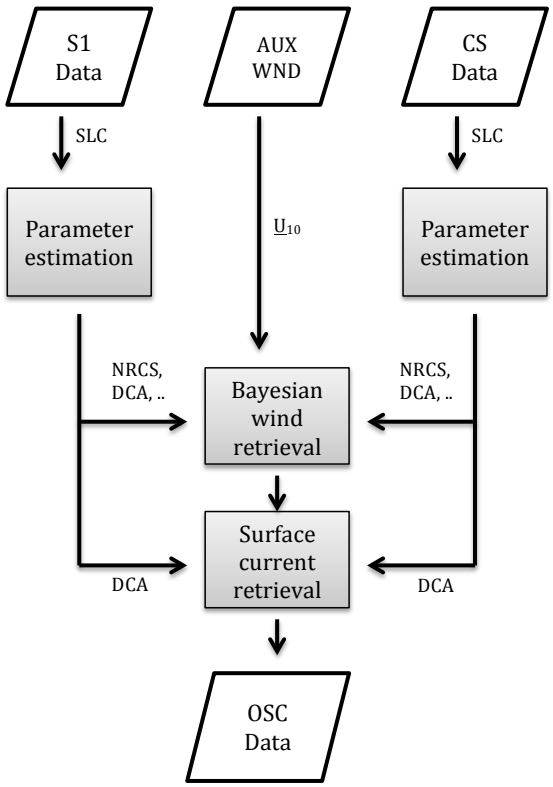

Figure 17 *: Flowchart of main processing units for surface current retrieval from S1+CS measurements.*

The direct inversion approach using model wind (ECMWF) field (both wind speed and direction) has been applied on Sentinel 1 data with an accuracy of the surface current of around 0.39 m/s when evaluated against surface drifters, and 0.6 m/s when evaluated against GlobCurrent and OSCAR model field (see Figure 18). The standard deviation observed between drifters and Sentinel 1A velocity is most likely a combination of errors in the wind field and in CDOP.

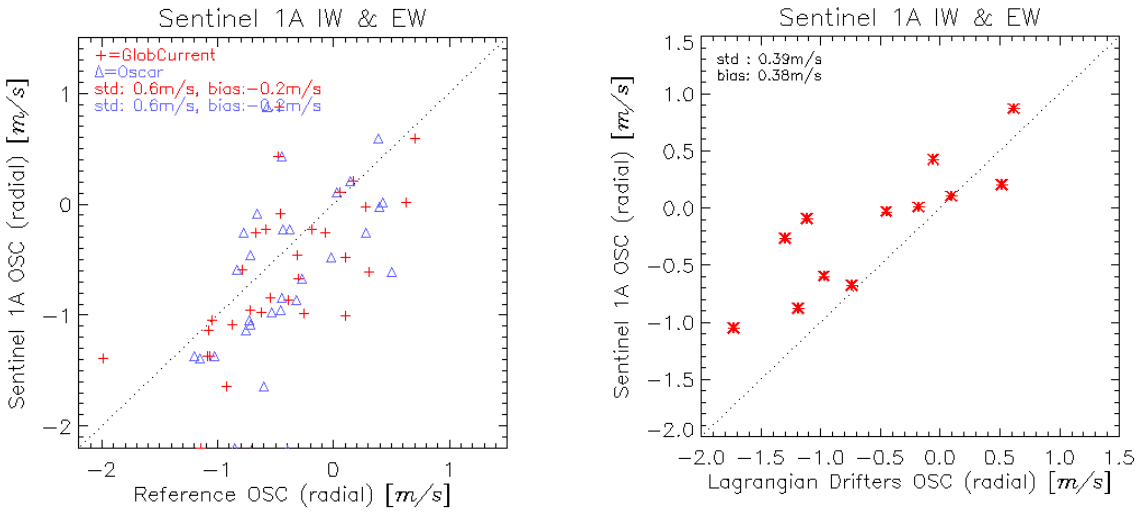

a) b)

Figure 18 *: Sentinel 1A radial surface current speed versus reference current speed, a) reference current speed from GlobCurrent and OSCAR, b) reference current speed from Lagrangian surface drifters.*

3.2.1. Cross-polarization

The S1+CS have the capabilities of measuring DCA and NRCS in both co- and cross-polarizations. The use of cross-polarization offers new perspectives for measuring both wind and surface velocity. The DCA in cross-polarization is expected to be less sensitive to sea-state than in co-polarization [14],[15]. Furthermore, the wind speed in cross-polarization is insensitive to wind direction and no external model wind direction is required. However, both the NRCS and the DCA signals are much smaller in cross-polarization than in co-polarization for mono-static backscattering, and requirements on precise calibration and noise correction will be stronger. However, for bi-static scattering the NRCS in cross-polarization is general much higher than in co-polarization.

Attempt to optimize combination of co- and cross-polarization for wind retrieval in wide swaths imaging is a research topic, but very promising results on improving the wind estimates at high winds using cross-pol data are achieved.

A synergetic approach for retrieval of wind and current by combining the co- and cross-polarization for S1+CS should be exploited to improve the wind and thus also the surface current retrieval. Such an approach has been demonstrated for synergetic wind and wave field retrieval [16].

An example of the Doppler anomaly in co- and cross-polarization from Sentinel-1A S1 data is shown in Figure 19. Note that a relatively strong Doppler anomaly signal is observed in the cross-pol channel in areas of strong backscatter. The noisy area in lower right part of the HV Doppler is due to low signal-to-noise ratio i.e. low backscatter.

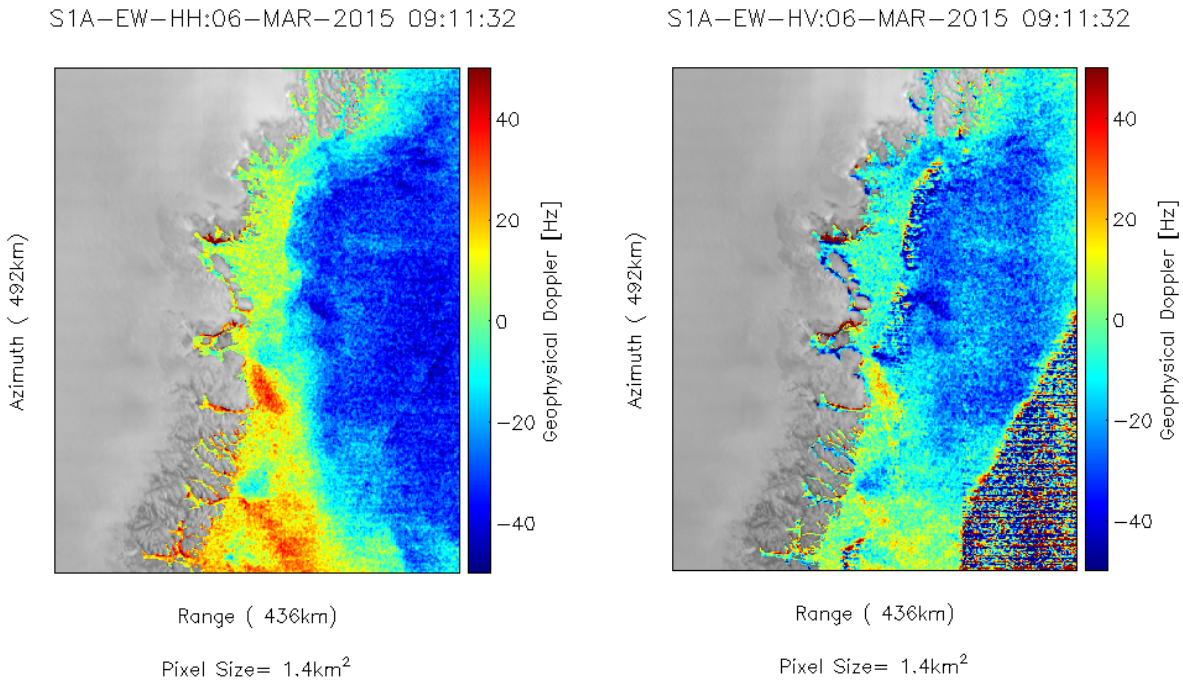

Figure 19 *: Sentinel 1A Doppler anomaly from dual-pol EW data, a) HH polarization, b) HV polarization.*

3.2.2. Uncertainties and Requirements

The accuracy of wind retrieval directly maps into the accuracy achievable for the surface current. In Figure 20 is shown how an uncertainty of the wind speed of 2 m/s in upwind and downwind translate into an uncertainty in the Doppler anomaly for different wind speeds between 5– 11 m/s. The relation is shown as function of incidence angle. The green dotted lines indicate that if we want to use the DCA estimate for wind retrieval only, the accuracy must be less than 2Hz to achieve and accuracy of wind speed of less than 2 m/s. Furthermore, it shows that the wind speed must be predicted better than 2 m/s for all wind directions if the goal is to have a surface current DCA with an accuracy better than 2Hz.

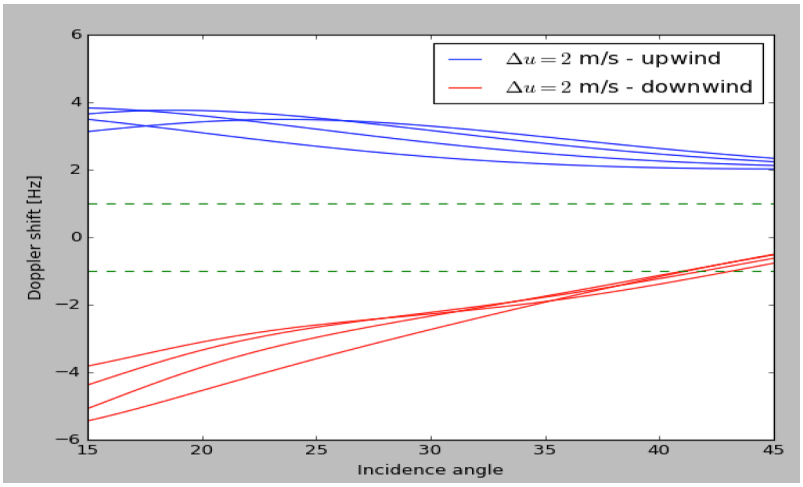

Figure 20 *: Doppler anomaly uncertainty versus an uncertainty of wind speed of 2 m/s in upwind and downwind for wind speeds ranging between 4 and 10 m/s [25].*

An uncertainty in the DCA directly maps into an uncertainty in the radial component of the surface current through Eq.(17), and shown in Figure 21. The uncertainty in the Doppler comes from uncertainties in the measured DCA as well as in the predicted wind/wave induced DCA. We see that a 5Hz uncertainty translates into a 30 cm/s uncertainty in the velocity at about 27^{o} incidence angle. A Doppler anomaly accuracy of ≤ 2 Hz is required for accuracy in current velocity of $\leq$10 cm/s.

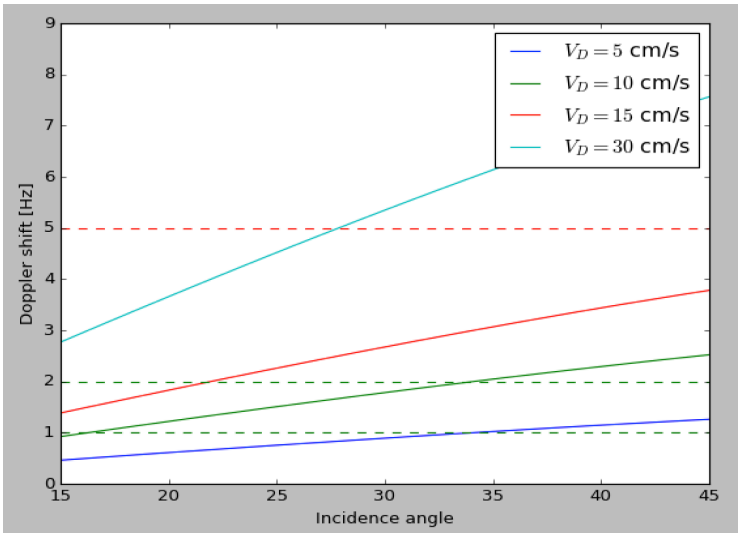

Figure 21 *Doppler anomaly uncertainty and corresponding radial velocity uncertainty for different incidence angles [25].*

4. Recommendations for S1+CS study

The goal of the accuracy of the DCA from both S1 and CS is around 2Hz, defined by an accuracy of the surface current of around 0.1 m/s. This put strong requirements on the whole chain from system, processing, geophysical models and retrieval methodology. Below is specified some fundamental aspects that must be considered for a scientific study on S1+CS capabilities and limitations.

4.1. System Recommendations

The geophysical requirements also put requirements on the S1+CS system parameters such as NESZ, ambiguity, attitude and antenna. Some basic requirements that the system must provide are listed below:

- ✓ *Attitude data for computation of geometric Dc to the required accuracy.*
- ✓ *Antenna model for computation of Dc bias as function of elevation angle to the required accuracy.*
- ✓ *Noise vector range profile for correction of additive noise.*
- ✓ *Minimization of ambiguity*
- ✓ *Sufficient high-spatial single-look resolution to achieve the desired OSC resolution and standard deviation*

4.2. Product and Processing Requirements

The S1+CS system put some additional requirements on the SAR processing and Doppler estimation in order to meet the requirements set by the OSC estimation and retrieval.

- ✓ *The SAR processing must ensure maximum overlap between bursts in azimuth*
- ✓ *The SAR processing must provide a "clean" azimuth Fourier domain*
- ✓ *The Doppler processor must have access to updated antenna model data on a suitable form*
- ✓ *The Doppler processor must have access to attitude data on a suitable form*
- ✓ *The Doppler processor must provide a calibrated NRCS*
- ✓ *The Doppler processor must have access to noise vector in range at regular azimuth intervals (TBD)*
- ✓ *The Doppler processor must have access to collocated global wind field in near real-time for input to the OSC retrieval*
- ✓ *The Doppler processor must provide overlaps (at least one grid point) between swaths*
- ✓ *The Doppler processor must provide seamless estimates over bursts*
- ✓ *The Doppler processor must provide an estimate of the Doppler standard deviation on the same grid as the Doppler anomaly*
- ✓ *The Doppler processor must provide similar accuracy of Doppler for S1 and CS*

4.3. Doppler Performance and Calibration Requirements

The accuracy of the S1+CS Doppler estimator itself must be assessed:

- ✓ *Methodology and strategy to assess the accuracy of the Doppler estimate and the predicted Doppler standard deviation must be developed. Use of land areas of homogeneous backscatter (such as rainforest) is required. The predicted Doppler standard deviation should be compared with the data driven standard deviation computed from the grid of estimated Doppler values.*

Precise calibration of the Doppler is mandatory for achieving the required accuracy on the surface current. Attempts of modeling the deterministic contributions to the estimated Doppler centroid are at present not sufficient to reach the required accuracy of ≈ 2Hz. Proposed research activity is listed below:

- ✓ *Research should be undertaken to explore other methods (internal) to monitor and absolute calibrate the Doppler centroid i.e. to better estimate the attitude DC variations with time around the orbit. One approach could be to exploit the cross spectral properties in relation to the Doppler anomaly in a data driven approach. The S1 WV data could be used for this.*

4.4. Geophysical Models and Inversion

The S1+CS constellation requires development of appropriate geophysical model function (and the corresponding inverse model) for both NRCS and Doppler anomaly. For the Sentinel 1 mono-static measurements the project should take benefit of the GMF developed for co- and cross-pol data. Some required research activities are listed below:

- ✓ *For the CS bi-static measurements new GMF functions must be developed for both NRCS and the Doppler anomaly in different polarizations. A starting point could be the existing physical based backscattering models in bi-static geometry.*
- ✓ *The GMF should better address the effects of wave field on the DCA*
- ✓ *The inversion model should take benefit of the latest Bayesian approach combining the several metrics (i.e. NRCS, DCA, Wave Spectra) from mono- and bi-static geometry in an optimal way.*
- ✓ *Of importance is also to optimize the combination of co- and cross-pol measurements both for wind and surface current retrievals.*

4.5. End-to-End Simulation

A simulation toolbox should be developed for performing an end-to-end simulation, from data acquisition to the final ocean surface current product. Following points to considered are:

- ✓ *Develop simulation model and tools for generating S1+CS raw data representing realistic ocean dynamics (both waves and current) and system noise statistics*
- ✓ *Develop processing algorithms for generating high-resolution DCA and NRCS products from the simulated raw data*
- ✓ *Develop an inversion model and tools for inverting the S1+CS DCA and NRCS into a surface current product*
- ✓ *Perform an assessment of performance by comparing the input an output ocean surface current.*

4.6. Assessment of Surface Current Retrieval Performance

Assessment of the performance of surface current retrieval from S1+CS DCA and NRCS measurements involves quantifying accuracy of both instrumental and geophysical/retrieval terms. We shall however, assume that the DCA (or RVL) and NRCS are calibrated to within the required accuracy. The following strategy could then be considered to assess the different OSC retrieval error sources:

- ✓ *Evaluate the forward GMFs for NRCS and DCA (or RVL) in both mono- and bi-static geometry. This can be achieved by comparing the simulated values against measured values using collocated ground truth of wind, wave and current fields from selected supersites. Dedicated bi-static campaign is needed in order to establish this data set. Quantify the errors (bias and variance) as function of for instance wind speed and direction, wave height, and surface current speed and direction. This must be done for different imaging geometry (swaths) and polarizations.*

- ✓ *Quantify how errors in the input geophysical parameters (wind, wave, current) map into error in the NRCS and DCA and vice versa through the respective forward and inverse GMFs, respectively. This can be achieved by running the forward and inverse simulations*

with and without small perturbation in the input parameters. Again, this must be done for different imaging geometry (swaths) and polarizations.

- ✓ *The performance of the Bayesian retrieval itself can be established by using a realistic synthetic data set including noise, or a real data set with good ground truth. The simulated data set can be generated from the forward models with noise added, and covering the expected range of wind, wave and current. These data sets can be inverted by the Bayesian retrieval and the output can be evaluated against the input.*

5. References

1. B. Chapron, F. Collard, F. Ardhuin, "Direct measurements of ocean surface velocity from space: Interpretation and validation", J. Geophysical Research, Vol. 110, No. C7, pp. 10.1029, 2005
2. J. A. Johannessen, B. Chapron, F. Collard, V. Kudryavtsev, A. Mouche, D. Akimov, K. F. Dagestad, "Direct ocean surface velocity measurements from space: Improved quantitative interpretation of Envisat ASAR observations", Geophysical Research Letters, Vol. 5, doi:10.1029/2008GL035709, 2008
3. A. Mouche, F. Collard, B. Chapron, K. F. Dagestad, G. Guittion, J. A. Johannessen, V. Kerbaol, M. W. Hansen, "On the use of Doppler shift for sea surface wind retrieval from SAR", IEEE Trans. Geoscience and Remote Sensing, Vol. 50, pp.2901- 2909, doi:10.1109/TGRS.2011.2174998, 2012
4. T. Kræmer T., H. Johnsen, C. Brekke, "Emulating Sentinel-1 Doppler Radial Ice Drift Measurements Using Envisat ASAR Data", IEEE Trans. Geoscience and Remote Sensing, Vol.12, No.53, DOI: 10.1109/TGRS.2015.2439044, pp: 6407 – 6418, August 2015
5. Engen G., Johnsen H., Larsen Y., "Sentinel-1 geophysical Doppler product – performance and application", Proc. of EUSAR2014, Berlin, 3-5 June 2014
6. Engen G., Johnsen H., "Sentinel-1 Doppler and Ocean Radial Velocity Algorithm Definition", Norut Report No. 19/2015, S1-TN-NRT-53-0658, version 1.4, ISBN: 978-82-7492-311-9
7. G. Engen, H. Johnsen; SAR-Ocean Wave Inversion Using Image Cross Spectra, *IEEE Transc. on Geo. Science and Remote Sensing*, Vol. 33, No. 4, pp.1047-1056, 1995.
8. Faozi S., H. Johnsen, "Ocean surface wind retrieval from co-polarized SAR data using the polarization residual Doppler frequency", *IEEE Trans. Geoscience and Remote Sensing*, July 2013, Digital Object Identifier 10.1109/TGRS.2013.2278550
9. Johnsen H., Collard F., "SAR wave processing – improvements towards Sentinel-1 mission", Proc. of SeaSAR2012, 18-23 June 2012, Tromsø
10. Faozi S. , H. Johnsen, F. Nouguier, B. Chapron, G. Engen, "Onto a skewness approach to the generalized curvature ocean surface scattering model", submitted to *IEEE Trans. Geoscience and Remote Sensing* October 2014
11. Said F., Johnsen H., Chapron B., and Geir Engen, "An ocean wind Doppler model based on the generalized curvature ocean surface scattering model", *IEEE Trans. Geoscience and Remote Sensing*, Vol.53, No.12, DOI 10.1109/TGRS.2015.2445057, Dec 2015
12. G. Engen, I. Friestad-Pedersen, H. Johnsen, and T. Elfouhaily, "Curvature effects in ocean surface scattering," *IEEE Transactions on Antennas and Propagation*, vol. 54, no. 5, pp. 1370–1379, May 2006.
13. Pedersen F. I., Engen G., Johnsen H., "Polarization Dependency in Doppler Frequency Shift and its Application to Envisat ASAR Alt-Pol Data", Proc. ERS/Envisat Symposium, 6-10 Sept. 2004, Salzburg
14. Fois F., Hoogeboom P., Le Chevalier F., and Stoffelen A.. "An Analytical Model for the Description of the Full-Polarimetric Sea Surface Doppler Signature." Journal of Geophysical Research: Oceans 120, no. 2 (2015): 988–1015.
15. Fois, Franco, Peter Hoogeboom, François Le Chevalier, Ad Stoffelen, and Alexis Mouche. "DopSCAT: A Mission Concept for Simultaneous Measurements of Marine Winds and Surface Currents." Journal of Geophysical Research: Oceans, 2015. http://onlinelibrary.wiley.com/doi/10.1002/2015JC011011/full.
16. Zhang, Biao, Xiaofeng Li, William Perrie, and Yijun He. "Synergistic Measurements of Ocean Winds and Waves from SAR." Journal of Geophysical Research: Oceans, août 2015, n/a – n/a. doi:10.1002/2015JC011052.
17. Hwang, P. A., A. Stoffelen, G.-J. Van Zadelhoff, W. Perrie, B. Zhang, H. Li, and H. Shen (2015), Cross-polarization geophysical model function for C-band radar backscattering from the ocean surface and wind speed retrieval, J. Geophys. Res. Oceans, 120, 893–909, doi:10.1002/ 2014JC010439.
18. Zhang, B., and W. Perrie (2012), Cross-polarized synthetic aperture radar: A new potential technique for hurricanes, Bull. Am. Meteorol. Soc. 93, 531–541, doi:10.1175/BAMS-D-11-00001.1.
19. Vachon, P. W., and J. Wolfe (2011), C-band cross-polarization wind speed retrieval, IEEE Geosci. Remote Sens. Lett., 8(3), 456–459, doi: 10.1109/LGRS.2010.2085417.
20. Gerling, T. W., Structure of the surface wind field from the SEASAT SAR, J. Geophys. Res., vol. 91, 2308-2320, 1986.
21. Horstmann J., Lehner S., Kock W., Tonboe R., (2000), Computation of wind vectors over the ocean using spaceborne synthetic aperture radar, The Johns Hopkins Univ. Tech. Dig., vol. 21, no. 1, pp. 100–107.

22. Du Y., Vachon P.W., Wolf J., 2002, Wind direction estimation from SAR images of the ocean using wavelet analysis, Canadian J. Remote Sens., vol. 28, pp. 498–509.
23. Schulz-Stellenfleth J., Konig T., Lehner S., ―*An empirical approach for the retrieval of integral ocean wave parameters from synthetic aperture radar data*‖, Journal of Geophysical Research Vol. 112, C03019, 14 PP., 2007 doi:10.1029/2006JC003970
24. Mouche A., Chapron B., "Global C-band Envisat, Radarsat-2 and Sentinel1- SAR measurements in co-polarization and cross-polarizations", J. of Geophysical Research: Ocean, DOI: 10.1002/2015JC011149, Nov 2015.
25. Wergeland Hansen M., Engen G., Johnsen H., Johannessen J.A., Korosov A., " Improved measurements of mean sea surface velocity from SAR", Living Planet Symposium, 9-13 May, 2016, Prague
26. Bamler R., "Doppler frequency estimation and the Cramer-Rao Bound", IEEE Trans. Geoscience and Remote Sensing, Vol. 29(3), pp. 385–390, 1991
27. Cumming I. G., F. H. Wong": Digital processing of Synthetic Aperture Radar Data, Artech House, ISBN-13:978-1-58053-058-3, 2005
28. Hwang P.A., Fois F., "Surface roughness and breaking wave properties retrieved from polarimetric microwave radar backscattering", J. Geophys. Res. Oceans, 120, 3640-3657, doi:10.1002/ 2015JC010782.
29. Romeiser R. and D. R. Thompson, "Numerical study on the along-track interferometric radar imaging mechanism of oceanic surface currents," IEEE Transactions on Geoscience and Remote Sensing, vol. 38, no. 1, pp. 446–458, 2000
30. Kudryavtsev, V., D. Akimov, J. A. Johannessen, and B. Chapron (2005), On radar imaging of current features: 1. Model and comparison with observations, J. Geophys. Res., 110, C07016, doi:10.1029/2004JC002505.
31. Fois F., "S1+CS Selected Concept Performance Analysis Report", S1CS.ASU.SY.PR.0000X, Issue 2.0, 2016
32. Dragosevic M. V., Vachon P. W., "Estimation of ship radial speed by adaptive processing of Radarsat-1 fine mode data", *IEEE Transc. on Geo. Science and Remote Sensing*, Vol. 5, No. 4, pp.678-682, 2008.